Circulation and Dynamics of the Western North Atlantic. Part II: Dynamics of Meanders and Rings

A. R. ROBINSON AND A. GANGOPADHYAY*

Division of Applied Sciences, Department of Earth and Planetary Sciences, Harvard University, Cambridge, Massachusetts

(Manuscript received 26 April 1995, in final form 31 May 1996)

ABSTRACT

A multiparameter kinematic synthesis of multiscale feature models for the circulation of the western North Atlantic was developed in Part I of this study. The dispersion characteristics and dynamical behavior of this circulation model are presented here in detail. Insertion of the kinematically synthesized features into a numerical dynamical model dynamically adjust the features and provide the basis for a multiparameter sensitivity study with respect to the reasonable range of parameter variation consistent with observations. Two primary characteristics of the Gulf Stream meandering behavior, namely, the wave-growth characteristics and the ring formation and absorption statistics are studied via both quasigeostrophic and primitive equation dynamics. In achieving realistic dispersion characteristics, a comprehensive methodology for dynamical model tuning and validation in this limited region ocean is developed. The realistic regimes of parameter variation are identified on the basis of observational growth rate and phase speed of the Gulf Stream meanders. Long-term simulations within these realistic regimes provide statistics of ring production and interaction behavior. The observed range of transport variability of the Gulf Stream system further constrains the parameter selection. Final tuning of parameters is obtained through an extensive study of the response from the dynamical models to the changes of parameters of the circulation model. Usefulness of the circulation model for initializing, forecasting, and updating in real synoptic cases will be the focus of Part III of this series of studies.

1. Introduction

This is a study of wave-growth and ring production and reabsorption in the Gulf Stream and meander ring (GSMR) region. The study is carried out via the initialization of numerical dynamical models by a multiscale feature model (MSFM) representation of the regional circulation elements. The MSFM synthesizes the regional historical data. The elements of the feature model have been linked together via mass conservation, and the range of the parameters of the feature model are determined by the statistics of the variability of the regional hydrographic and velocity data (Gangopadhyay et al. 1997, hereafter cited as GRA). The purposes of this study are twofold: 1) to further constrain the parameter range via the observed statistics of the Gulf Stream (GS) waves and rings and 2) to determine the ability of the dynamical models to reproduce the statistics of the wave-growth and ring interaction dynamics data. The success in reproducing the statistics of synoptical dynamical wave and ring processes serves to validate and calibrate the dynamical models for realistic simulations and real-time forecasts for the region.

The verification of ocean models for realistic regional field estimation is an important technical subject of current research. Experiments such as DAMEE GSR (Data Assimilation and Model Evaluation Experiments Gulf Stream Region) (Willems et al. 1994; Lai et al. 1994) have been conducted by different modeling groups with the objective of quantifying the predictability of dynamical models and the impact of data assimilation on such capabilities. We distinguish here among validation, calibration, and verification. By model validation we mean simply that the model physics is appropriate to represent the regional phenomena and processes of interest. Model calibration is achieved via determination of necessary regional and computational parameters. Finally, the dynamical model set needs to be verified against two particular aspects of the regional circulation. First, statistical verification is established when the model results agree with past data of synoptic realizations and their evolution in a statistical sense. Second, synoptic verification is achieved when detailed agreement with actual synoptic realizations and evolutions is materialized. The validation of the Harvard model set used here was achieved during real-time Gulfcast op-

* Current affiliation: Department of Physics, University of Massachusetts—Dartmouth, North Dartmouth, Massachusetts.

Corresponding author address: Dr. Avijit Gangopadhyay, Center for Marine Science and Technology, University of Massachusetts—Dartmouth, 706 S. Rodney French Boulevard, New Bedford, MA 02744.
E-mail: avijit@atlantic.cmast.umassd.edu

erations as documented by Glenn and Robinson (1995). It is the calibration and statistical verification of the dynamical model sets that will be the focus of this study. In this study, we utilize both the Harvard primitive equation (PE) and quasigeostrophic (QG) models.

The circulation model for the western North Atlantic (WNA) region developed by GRA synthesizes the regional circulation elements and provides the bases for a powerful method of data assimilation and initialization into dynamical models and for quasi-analytical theoretical process studies. For dynamical model integrations of longer than about 2 weeks (simulations, forecasts, field estimates, process studies), such three-dimensional initializations are essential. Circulation feature models provide the basis for real data initialization from synoptic realizations, with minimal input of observational data and without prior dynamical model spinup. P. Malanotte-Rizzoli and R. Young (1997, manuscript submitted to *J. Atmos. Oceanic Technol.*) have studied the impact of assimilating global versus local synoptic datasets in a regional semispectral primitive equation model developed by Haidvogel et al. (1991). Simulations with different forcings have been studied by Ezer and Mellor (1992). Geosat data has been assimilated in the GS region by Mellor and Ezer (1991) and Glenn et al. (1991). The Harvard PE model has been used for operational forecasting (Robinson et al. 1989) in the GS region. In this study, we will show that the MSFM initialization renders a powerful and efficient way of calibrating and verifying any dynamical model for this region.

Since the circulation elements of the region under study have realistic data-based representations, the wave-growth study should be definitive. The circulation structures include the GS, the deep western boundary current (DWBC), the southern recirculation gyre (SRG), the northern recirculation gyre (NRG), and the slope water gyre (SLP). A schematic of the region is shown in Fig. 1. Parameterization of each of these features and the kinematic synthesis for initialization of a numerical dynamical model is discussed in detail in GRA. Table 1 shows the parameters and their ranges that are constrained by kinematics. In this study, the Harvard PE and the QG dynamical models have been calibrated for the GSMR region on the basis of several numerical experiments. The initial states for all numerical experiments in this study are guided by observations and kinematical balance. In each experiment, such initial states are dynamically adjusted, and the resulting fields are evolved in time via the dynamical models. Starting from a ''synoptic features at mean locations'' state, the circulation field evolves in time with certain characteristics of the real ocean. The model parameters are then calibrated by comparing the model behavior against the observed statistics of synoptical dynamics. There have been theoretical developments of dispersion models of *n*-layer fronts (Flierl 1991), and observational studies of GS meanders are limited to the region between Cape Hatteras and the Grand Banks (Tracey and Watts 1986; Lee and Cornillon 1996a). For this study, observed statistics of the rate of meander growth, the wavelength of such meanders, and the propagation rate are used. Short-term simulations are carried out to establish the dispersion characteristics of the PE dynamical model. The QG dynamical simulations yield similar results. The observed dispersion characteristics in the GSMR region are then used to identify the realistic parameter regime of the multiscale feature model set.

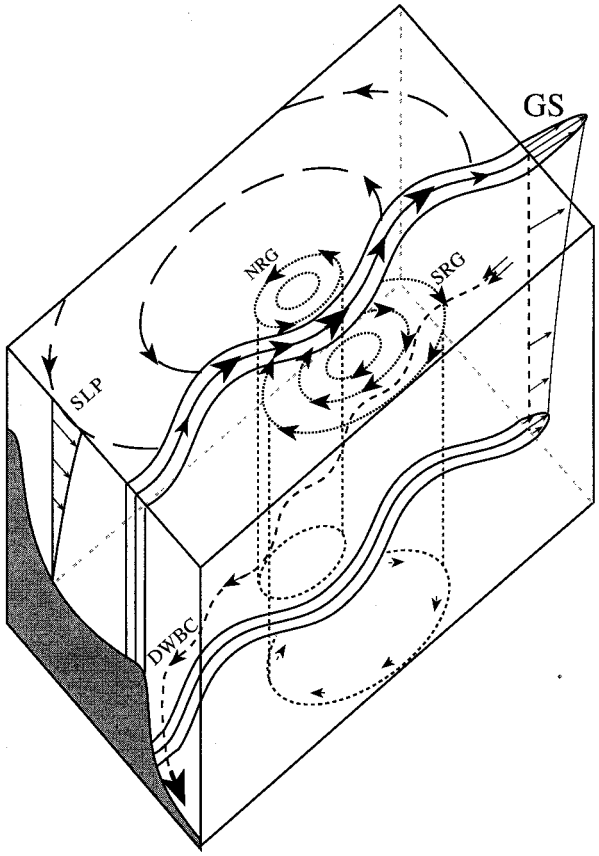

FIG. 1. Schematic of the prevalent features in the Gulf Stream meander and ring (GSMR) region: Gulf Stream (GS), deep western boundary current (DWBC), northern recirculation gyre (NRG), southern recirculation gyre (SRG), and slope water gyre (SLP).

In this study, we have achieved the capability of generating long-term realistic simulations for up to 12–15 weeks with realistic dispersion and ring-formation statistics for the GSMR region. Longer than 15 weeks, the large-amplitude meandering and nonlinearities of the dynamical system surpass the reliability of the dynamical model evolutions. Once the parameter space for realistic dispersion characteristics is established, the most important controlling parameters of the multiscale feature model are varied within the realistic wave-growth regime for studying the longer-term dynamical behavior of the stream and the background features. For both meandering and ring statistics, the model performance is compared with respect to known observational

TABLE 1. Central set of multiscale circulation model parameters.

Parameter	Value	Range	Comment
g_n	45 km		GS width in the slope side
g_1	40 km		G1 width in the Sargasso side
g_2	110 km		G2 width in the Sargasso side
U_H^T	1.30 m s^{-1}	1.0–1.5 m s^{-1}	GS top velocity at Cape Hatteras
U_H^B	0.0 m s^{-1}	0.0–0.5 m s^{-1}	GS bottom velocity at Cape Hatteras
Z_{lnm}	4600 m		Level of no motion
S_{tilt}	30 km	15–30 km	GS axis tilt
Z_{tilt}	800 m	700–1000 m	Depth of maximum tilt
g_W^n	50 km		DWBC northern width
g_W^s	50 km		DWBC southern width
Z_{DWBC}^T	800 m		DWBC shallowest depth
Z_{DWBC}^B	4600 m		DWBC bottom depth
U_{DWBC}^T	0.0 cm s^{-1}		DWBC velocity at Z_{DWBC}^T
U_{DWBC}^B	20 cm s^{-1}	15–40 cm s^{-1}	DWBC velocity at Z_{DWBC}^B
$C_{\text{SRG}}^{\text{lon}}$	60°W		Longitude for SRG center
$C_{\text{SRG}}^{\text{lat}}$	38°N		Latitude for SRG center
A_{SRG}	700 km		SRG major axis
B_{SRG}	500 km		SRG minor axis
U_{SRG}^T	7 cm s^{-1}	6–10 cm s^{-1}	SRG velocity at Z_{SRG}^T
U_{SRG}^B	2 cm s^{-1}	2–5 cm s^{-1}	SRG velocity at Z_{SRG}^B
$C_{\text{NRG}}^{\text{lon}}$	56°W		Longitude for NRG center
$C_{\text{NRG}}^{\text{lat}}$	42.4°N		Latitude for NRG center
A_{NRG}	500 km		NRG major axis
B_{NRG}	100 km		NRG minor axis
U_{NRG}	3.5 cm s^{-1}	3–5 cm s^{-1}	NRG barotropic velocity
$C_{\text{SLP}}^{\text{lon}}$	62°W		Longitude for SLP center
$C_{\text{SLP}}^{\text{lat}}$	40°N		Latitude for SLP center
A_{SLP}	1800 km		SLP major axis
B_{SLP}	400 km		SLP minor axis
U_{SLP}	3 cm s^{-1}	3–6 cm s^{-1}	SLP top velocity

behavior statistics. Finally, we discuss the model results with respect to observed transport variability in the GS system and infer a set of parameter values that are used for forecasting real synoptic cases.

In the following section, we describe the issues involved in initialization and choice of parameters. Two important sensitivities, computational parameters and the choice of inclusion/exclusion of DWBC, are included in this section. In section 3, the dispersion characteristics obtained from 3-week-long simulations are presented. The long-term simulations to study the dynamical behavior of the GS system via both PE and QG dynamics are described in section 4. Section 5 summarizes and presents conclusions.

2. Initialization issues and simulation parameters

For the purpose of this study, dynamical models are initialized via the multiscale feature models in the GSMR region. The adopted mean axes of the GS and the DWBC are described first with an example initial state. The subgrid-scale parameterization of the horizontal diffusion is very important for realistic behavior in the long term and is discussed in section 2b. The sensitivity of the behavior to the DWBC is presented next. Finally, the rationale behind the choices of particular multiscale parameters involved in this study is presented before discussing the model simulation results in the next two sections.

a. The initial state—A synoptic-stream climatology

The initial state is chosen to be the mean-axis, synoptic-stream configuration described in GRA. This state has no rings and the subbasin-scale (SBS) gyres are placed in their mean adaptation to conform to the mean axis of the GS. It is a regional circulation model based on climatological gyres and the climatology of the synoptic GS structure, which we call the ''synoptic-stream climatology.'' This configuration provides a useful basis for dynamical model calibration, as well as describes a synoptic climatological state of the western North Atlantic, which was described in GRA.

For all of the numerical experiments, the initial state has the same mean GS axis whose irregularities provide background perturbations. This mean stream axis is derived from 12 years (1975–86) of satellite Advanced Very High Resolution Radiometer data over the western North Atlantic (Gilman 1988). This is shown in Fig. 2, along with the underlying topography and the historical mean path of the DWBC (Hogg et al. 1986). The synoptic structure of the GS at 73°W (Halkin and Rossby 1985) is adopted on the mean axis at Cape Hatteras, while the kinematical synthesis of the surrounding mean gyres will enhance the transport and structure of the GS farther downstream (see GRA for details).

For this initial state the DWBC has been maintained at 3400-m isobath until it crosses under the GS to the 4200-m isobath. Such a configuration conserves the po-

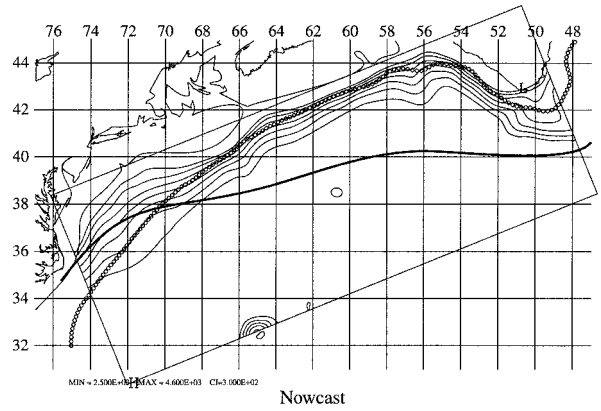

FIG. 2. Mean Gulf Stream path (obtained from average SST between 1977 and 1988) and the climatological DWBC path over topography in the model domain.

tential vorticity of this thermohaline jet in the Hogg and Stommel (1985) sense. The southern, northern, and slope gyres are slightly deformed with mass conserving constraints described in GRA. It is important to note that this initial state does not contain any ring; only the synoptic GS at its mean position and other mean features deformed slightly to adhere to the synoptic-stream climatology configuration.

The kinematically synthesized circulation fields are first dynamically adjusted for 1–3 days by the QG dynamical model. The resulting streamfunction and vorticity fields are then utilized along with a water-mass model (GRA) to obtain the initial primitive variables for the PE model. This methodology of QG adjustment before PE dynamics is called the ''slow-manifold'' initialization and adopted here for all numerical experiments described here. Such dynamical adjustment balances the kinematically synthesized fields, and filters out any spurious gravity wave modes that may otherwise be present.

A typical slow-manifold initialization for the PE model is shown in Figs. 2 and 3. The initial temperature field for the kinematically synthesized and 3-day, QG-adjusted, PE initialization is shown in Fig. 3. The top-left panel shows the GS dominating the upper thermocline circulation. The top-right panel shows the DWBC at 1800 m, partially recirculating with the stream and partially crossing underneath the stream. Observational evidence of such partial influx of DWBC water into the deep GS system is recently documented and studied by Pickart and Smethie (1993). Note that in the deepest level of 3900 m, the GS is entirely created by the southern and northern recirculations, which is shown in the bottom left panel. At this level, the DWBC is seen to cross the GS as a whole near Cape Hatteras and the stream is the narrowest and weakest there. The right panel at the bottom of Fig. 3 shows the temperature field at 50 m after being dynamically adjusted for 3 days. There is little change in position, but the adjustment between 74° and 72°W is clearly evident, which is due to the interaction between the DWBC and the GS at the initial stages of model evolution. Such adjustment will be discussed in detail in section 2c.

The resulting temperature and velocity sections of the initial state are shown in Fig. 4. Figure 4a shows the temperature section at initialization through 56°W. The

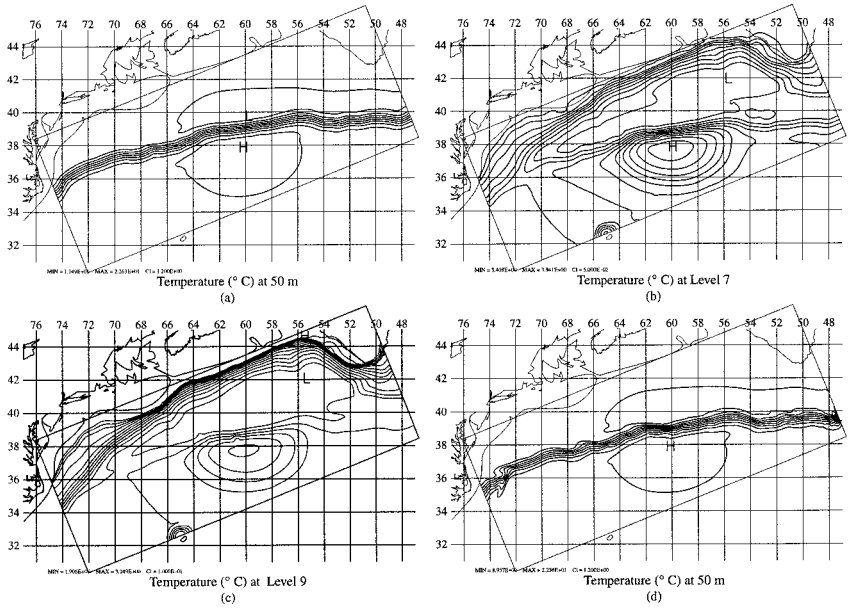

FIG. 3. PE model initialization and adjustment of the mean state in the GSMR region: (a) initial temperature at 50 m, (b) initial temperature at 1800 m, (c) initial temperature at 3900 m, and (d) 3-day dynamically adjusted temperature at 50 m.

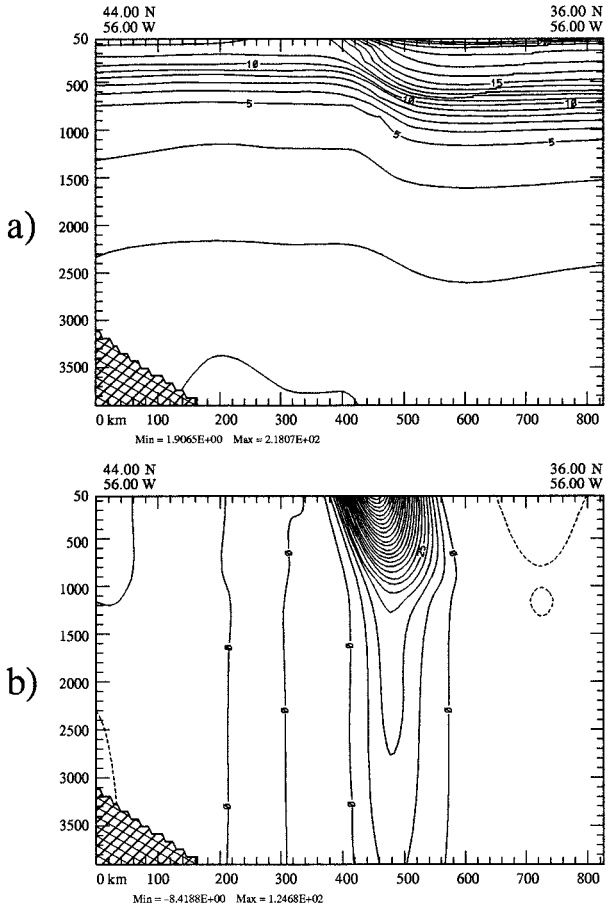

FIG. 4. (a) A typical north–south temperature section at initialization via the WNA circulation model and (b) a typical zonal velocity section across the same section as in (a).

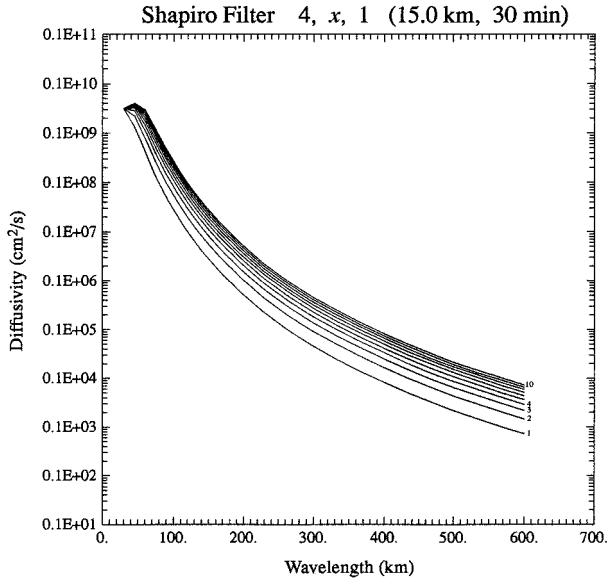

FIG. 5. Eddy diffusivity equivalence for fourth-order Shapiro filter.

corresponding zonal velocity section in Fig. 4b shows the GS, the recirculating gyres, and the DWBC signatures clearly. The sloping isotherms in Fig. 4a are derived from the initial streamfunction field via a water-mass model discussed in GRA. The little undulation in the temperature field in the northernmost part of Fig. 4a near the 2500-m isobath indicates the presence of the DWBC in that region. The combination of the slope and the northern recirculation gyre to the north of stream is identifiable in the slithering of the isotherms and the isotachs in Figs. 4a and 4b.

Such an initial realization, when allowed to dynamically evolve, would result in mesoscale interactions between the GS and the surrounding gyres. Such interactions occur over various timescales and periods. The stream meanders, the meanders grow when instabilities set in, topographic interactions occur, and large meanders are formed with crests and troughs that then detach from the stream into mesoscale rings. The model's ability to replicate such natural processes in its evolution is a major achievement of this study. For the synoptic-stream climatological configuration, preliminary wave growth occurs in the first 3 weeks of the dynamical simulations. In the next 4–6 weeks the evolution becomes dominated by meandering and mesoscale ring formations. These rings propagate westward and interact with the stream. Some of them get reabsorbed in the meandering stream, and some propagate out to the open regions, presumably to get absorbed by the Florida current or to decay in the Sargasso waters. Such wave-growth and ring–stream interaction statistics are the focus of the study here.

b. Eddy diffusivity parameterization

The horizontal eddy diffusivity in both of the dynamical models (PE and QG) is parameterized by a Shapiro filter (F_{npq}; order, number of repetitive applications, and frequency of application). A Shapiro filter of order four is equivalent to a second-order horizontal Laplacian on the velocity field for the dynamical models. The adaptation to this scale-selective smoothing operator (Shapiro 1970, 1971) is illustrated by Spall and Robinson (1990). To calibrate the dynamical models (both QG and PE) for the western North Atlantic, a series of numerical experiments were carried out by varying the filter order, number, and frequency. The width of the GS was maintained correctly for a period of over 3 months for a (4, 5, 1) Shapiro filter. The effective diffusivity increases with number of applications for a particular scale (wavelength), whereas it decreases for intermittent applications. However, intermittent application of the filter allows for growth of unwanted short wavelengths (two–three grid size), which then translates into unphysical features in the primary field of interest. The direct dependence on the different wavenumbers of the filter (4, 5, 1) is shown in Fig. 5 as a function of equivalent eddy viscosity coefficients (Lozano 1994,

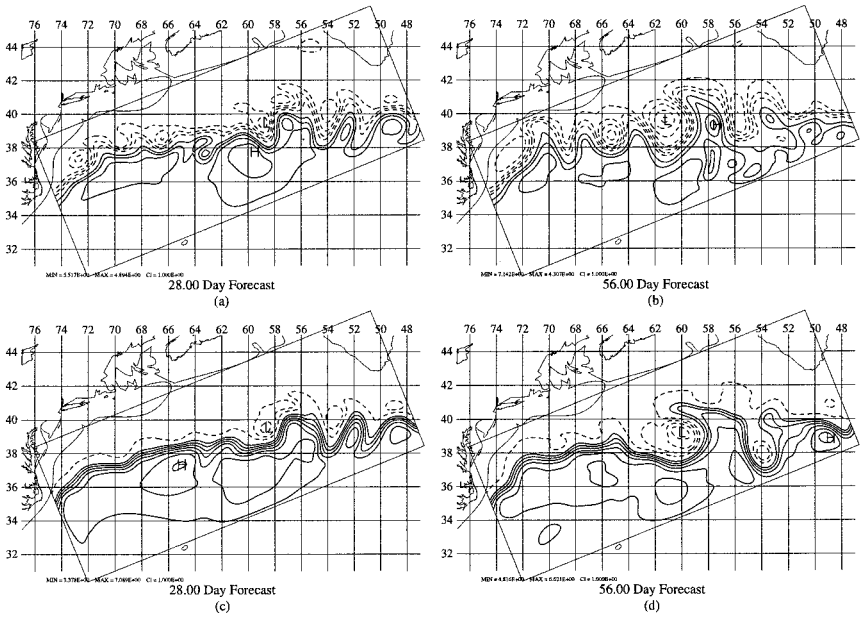

FIG. 6. Adjustment with or without DWBC: (a)–(b) 56-day simulation with DWBC and (c)–(d) 56 days into the simulation without DWBC.

personal communication). For the GS simulations, the effective eddy viscosity was found to be on the order of 10^5 cm^2 s^{-1} range for the relevant time step (15 min) and grid spacing (15 km). The choice of the time step and grid spacing for the GSMR region is obtained on the basis of computational efficiency; see description in Glenn and Robinson (1990).

c. Deep western boundary current effects

In this section, we investigate the sensitivity of the dynamical model due to the effects of the DWBC. The DWBC is modeled to carry a transport of 20 Sv southwestward along the 3400-m isobath in this study. Near Cape Hatteras it crosses under the GS while preserving its potential vorticity in the Hogg–Stommel (1985) sense. In the initial stages of adjustment via the dynamical model, these two currents interact with each other at the crossover region, and the initial wave growth of the stream, especially in the region 74°–70°W, is sensitive to such interactions.

To demonstrate this sensitivity, results from two numerical experiments are presented in Fig. 6. The DWBC, which is present in the first experiment, is considered nonexistent in the second. Both of these initializations were then driven by quasigeostrophic dynamics for 8 weeks. The stream gradually starts to meander evolving from its mean axis configuration and forms its first cold core ring by day 28 in the first experiment. The QG streamfunction on days 28 and 56 for this experiment is shown in Figs. 6a and 6b. The corresponding evolution for the second experiment, where the DWBC is nonexistent, is presented in Figs. 6c and 6d. Clearly, there are noticeable differences in the meandering evolution to the west of 60°W. To the east of 60°W the evolutions are quite similar during the first half of the simulation; there are, however, noticeable differences later in the simulation, which were affected by propagating meanders of different characteristics.

The major difference between the two simulations is the absence of interaction at 73°W, where the trough of the first meander is seen to form in Fig. 6a. The following trough is around 69°–68°W, giving rise to typical meander formation with 300-km wavelengths. Note also the meandering of the GS looks more realistic in Figs. 6a,b than in Figs. 6c,d, with its tight recirculations between the troughs and the crests. The first cold ring forms in the first experiment by 4 weeks at 63°W, whereas only a trough forms at the same location in the second simulation. The recirculation cells in between the troughs and crests are more realistic in the first simulation than those in the second simulation.

For the second simulation, a much longer wave (of wavelength around 400 km) starts to grow that develops a crest at 72°W, and the following trough is around 69°–70°W. Interestingly, for both of these simulations a trough forms at 69°–70°W, consistent with observational evidence of a trough at 68°–67°W (Johns et al. 1995; Watts et al. 1995). However, the QG simulations that included the DWBC seem to develop the trough closer to reality, both geographically and amplitude-wise.

The effect of inclusion/exclusion of DWBC is of importance to real-time nowcasting–forecasting. One could design a sensitivity of forecasting to the parameters of the DWBC, but it would be prudent to study

such sensitivities once other parameters of the multiparameter circulation model are chosen with proven capabilities of producing realistic wave-growth and dynamical behavior. In light of the above, all experiments analyzed hereafter are based on initializations that incorporate a 20-Sv DWBC as in the first simulation described here.

d. Feature model parameter selection

Recent observational studies (Halkin and Rossby 1985; Sato and Rossby 1992) have indicated that the transport of the GS in the upper 2000 m has a marginally significant seasonal variation. The maximum transport occurs in late spring–early summer, while the minimum is observed during wintertime, which is in agreement with Worthington (1976). According to Sato and Rossby (1992), the 0–2000-dB integral of the potential energy anomaly weighs the main thermocline fluctuations much more heavily, and, therefore, the potential energy anomaly on the Sargasso side shows a maximum seasonal signal during the spring. Conversely, the potential energy anomaly on the slope side has a minimum during early summer. As a combination of these two, the transport reaches a maximum in summer. The seasonal variability in the transport is about 17 Sv at 73°W (Halkin and Rossby 1985) with a mean of 87 Sv.

As mentioned in GRA, the number of degrees of freedom to characterize the synoptic state of the ocean via the multiscale parameterizations has been reduced to five. These are the surface velocity of the GS at Hatteras, the surface and bottom velocities of the SRG, the barotropic velocity of the NRG, and the surface velocity of the SLP. Based on the observational evidence as outlined above, the velocities for the two northern gyres, U_{NRG} and U^T_{SLP}, are conservatively set to their central values as listed in Table 1.

Given the fixed choices of parameters for DWBC, NRG, and SLP, the transport variation of the GS system is presented in Fig. 7. The transport variation at Cape Hatteras for different choices of U^T_H and U^B_H ranges from 50 to 100 Sv and is shown in Fig. 7a. The choices of SRG velocities and transport are shown in Fig. 7b. The maximum transport of the model GS is at 60°W, which comprises individual contributions from the three surrounding gyres. The transport at 60°W is given by Eq. (15) of GRA as follows:

$$T_{\mathrm{x60}} = T_H + T_{\mathrm{SLP}} + T_{\mathrm{NRG}} + T_{\mathrm{SRG}}. \quad (1)$$

Here,

$$T_H = \Gamma_{\mathrm{GS}}\Phi_H U^T_H, \quad (2)$$

$$T_{\mathrm{SLP}} = \Gamma_{\mathrm{SLP}}\Phi_{\mathrm{SLP}} U^T_{\mathrm{SLP}}, \quad (3)$$

$$T_{\mathrm{NRG}} = \Gamma_{\mathrm{NRG}} H U_{\mathrm{NRG}}, \quad (4)$$

and

$$T_{\mathrm{SRG}} = \Gamma_{\mathrm{SRG}}[\Phi_{\mathrm{SRG}}(U^T_{\mathrm{SRG}} - U^B_{\mathrm{SRG}}) + H U^B_{\mathrm{SRG}}]. \quad (5)$$

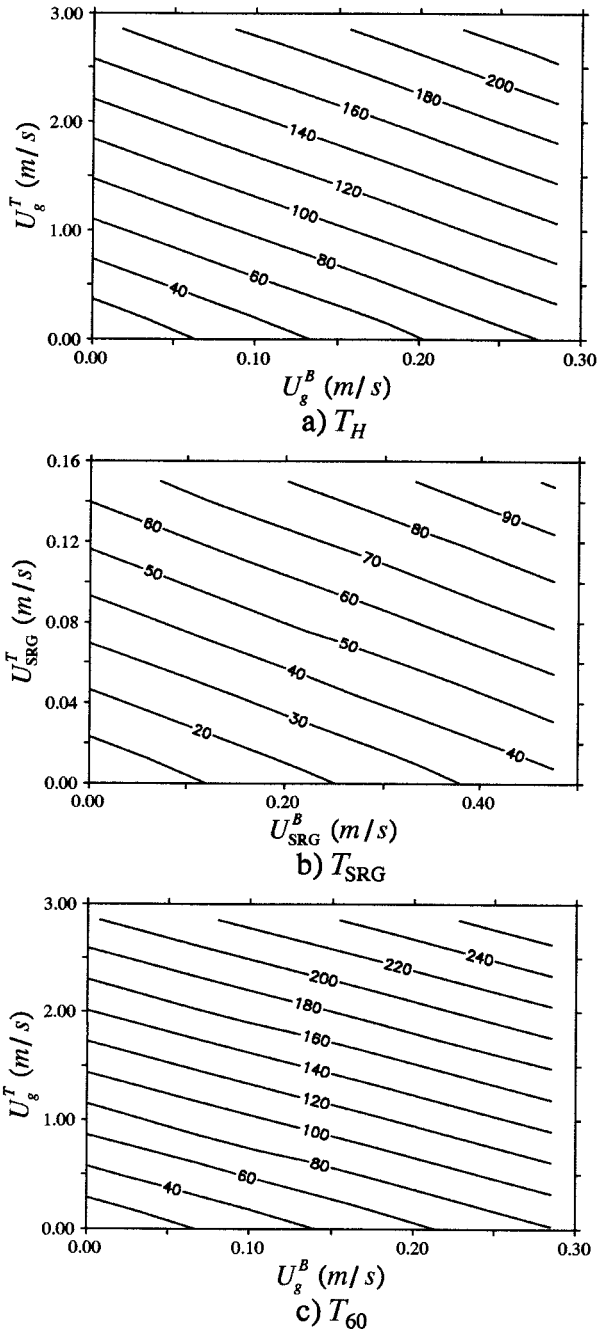

FIG. 7. Transport as a function of top and bottom velocities: (a) Gulf Stream at Cape Hatteras, (b) SRG, and (c) Gulf Stream at 60°W.

Using the numbers in Table 1 and values for multiscale interaction integrals (Γ, Φ), from GRA (Table 3), the transport variation for the stream at 60°W is determined and shown in Fig. 7c. As mentioned earlier, in this study, we chose to keep the SLP and NRG parameters as fixed throughout all experiments. The three parameters that are varied are U^T_H, U^T_{SRG}, and U^B_{SRG}. Using the simulations and analyzing them in the three-param-

TABLE 2. Results of the PE wave-growth analysis.

Expt	Shear at CH (cm s^{-1})	U^T_{SRG} (cm s^{-1})	U^B_{SRG} (cm s^{-1})	Shear of SRG	Wave growth (days)	Phase speed (km day^{-1})
172	100.0	7.0	2.0	5.0	22.00	5.62
112	100.0	10.0	2.0	8.0	18.00	6.08
115	100.0	11.5	5.0	6.5	13.90	11.25
132	130.0	7.0	2.0	5.0	6.29	8.00
139	130.0	9.5	3.5	6.0	6.95	11.25
132	130.0	10.0	2.0	8.0	5.80	16.87
133	130.0	10.0	3.5	6.5	12.20	11.25
135	130.0	11.5	5.0	6.5	5.45	16.87
137	130.0	13.0	7.0	6.0	18.00	14.06
157	150.0	7.0	2.0	5.0	9.80	11.25
151	150.0	10.0	5.0	5.0	18.31	22.50
155	150.0	12.0	5.0	7.0	18.29	19.80
177	170.0	7.0	2.0	5.0	14.00	19.70
179	170.0	9.5	3.5	6.0	7.60	12.50
175	170.0	12.0	5.0	7.0	13.90	21.37

eter space, we can identify the realistic parameter variation ranges for the MSFM set.

3. Dispersion and wave-growth characteristics

In this section, we deal with the dispersion characteristics, that is, the phase-speed and wave-growth statistics determined from dynamical mode simulations. The MSFM for the initial state is represented by the set of parameters listed in Table 1. The model behavior should be realistic, and its statistics should agree with the observed numbers. Our objective here is to identify the possible ranges of parameter variation that result in the most realistic dynamical model behavior of the GSMR region. Our approach is to carry out a series of short-term numerical model simulations over a possible range of parameter choices. The simulations are carried out by using the Harvard PE model described by Spall and Robinson (1989). Each initial state for a particular choice of parameters is obtained from the MSFM described in GRA. It has been observed that meanders of realistic wavelength and amplitudes develop in the first 3 weeks of the model run.

To determine the dispersion characteristics, a set of 15 experiments were carried out. The parameter variation of these experiments and resulting dispersion are listed in Table 2. The parameters were varied in such a way that the resulting wave-growth and phase-speed values can be interpolated and mapped as a continuous function of the independent variables.

a. Determining the growth rate and phase speed

An example of typical growth of meandering in the GSMR region is shown in Fig. 8. The initial wave growth and meandering is shown for days 12 to 18 at every 2-day interval. We center our attention to the region 72°–68°W for the first realistic wave growth. First, the wave crests and the troughs are identified, and the wavelength and amplitudes are measured quantitatively on the first day of the observed growth period. Similar evaluations are obtained for two successive 2-day intervals. The average values of the wave-growth characteristics during this period are then obtained as the final result.

A schematic representation of such meandering wave-growth is illustrated in Fig. 9. In this figure, the meander AB is identified with a characteristic wavelength L, cen-

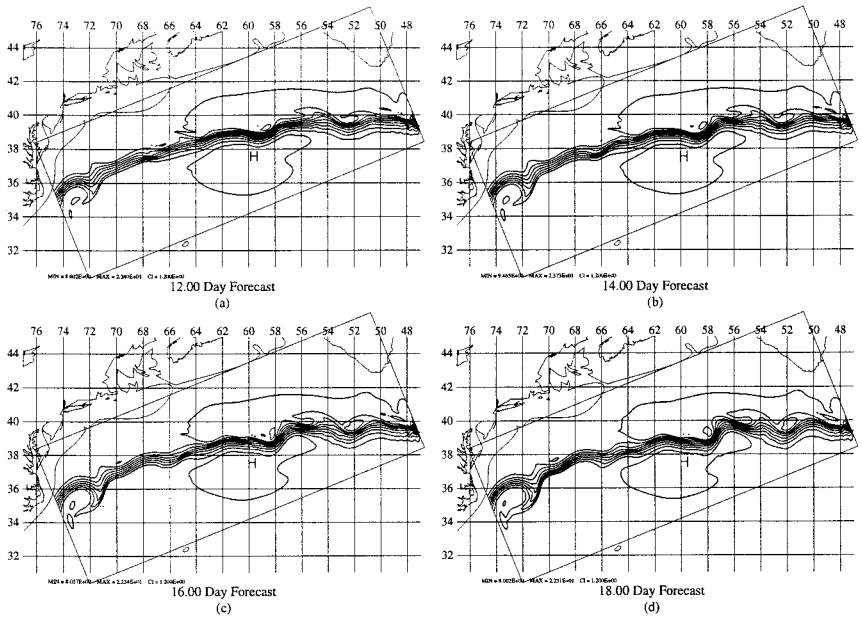

FIG. 8. An example of wave-growth and phase-speed computation: 20-day simulation.

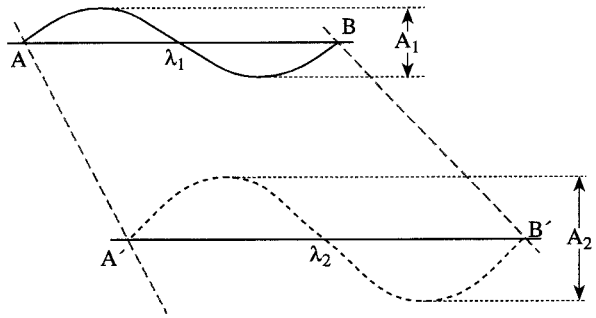

FIG. 9. Schematic of wave-growth computation. See text for explanation.

tered at a longitude λ_1. The amplitude of this meander is A_1 at time t_1. At a later time, t_2, the same meander is identified at λ_2 with a different wavelength L_2 and an amplitude A_2. In all of the 15 experiments, the region was chosen between 72° and 68°W, just northeast of Cape Hatteras.

Based on the above parameterizations, the growth rate t_0 is given by the following relationship:

$$A_2 = A_1 e^{(t_2 - t_1)/t_0} \tag{6}$$

or

$$t_0 = (t_2 - t_1)/\ln(A_2/A_1), \tag{7}$$

and the phase speed is given by the average speed at which the meander AB shifts to the position of meander $A'B'$ during the period $t_2 - t_1$. In other words, it is the ratio of the average of the differential longitudinal shifts between A and A', B and B', and λ_1 and λ_2 over the period of time $t_2 - t_1$.

It is important to note that for all of the 15 experiments, the wavelengths were in the range of 250–350 km with no distinguishable character. We, therefore, do not report the individual wavelengths to avoid redundancy. The measured range of wavelength agrees well with past observational studies in this region (Gangopadhyay et al. 1987; Gilman 1988). The evaluated phase speed and growth rates from all 15 experiments in the region 72°–68°W are listed in Table 2 and discussed in the next section.

b. Realistic regimes of growth rate and phase speed

The two dispersion characteristics, growth rate and phase speed, are presented as functions of the independent parameters in Fig. 10. The left panels show the variation of growth rate against the SRG parameters for different choices of GS axis velocity variation at Cape Hatteras. The right panel shows the model behavior of phase-speed variation as a function of different SRG parameters and the top velocity of the GS at Cape Hatteras. The axis velocity of the GS (U_H^T) is varied between 100 and 170 cm s^{-1}, which corresponds to a transport range of 56–90 Sv at Cape Hatteras for the GS. It is interesting to note that the growth rate increases with increasing U_H^T at Cape Hatteras up to about 110 cm s^{-1}, beyond which it decreases to a plateau of 6–8 days around 130–140 cm s^{-1}, and finally increases again with U_H^T. The phase speed is found to monotonically increase up to 24 km day^{-1} for a U_H^T of 150 cm s^{-1} at Cape Hatteras.

Observations of meander growth rate and phase speed have been studied by several investigators in the past (Watts 1983; Vazquez and Watts 1985; Tracey and Watts 1986; Lee and Cornillon 1996a,b). The wavelengths are observed to be around 300 km downstream of Hatteras (Gangopadhyay et al. 1987; Gilman 1988; Lee and Cornillon 1996b). In the region of study, a range of phase speed of 8–12 km day^{-1} is established as realistic objective for the numerical dynamical model, which agrees well with observations (Kontoyiannis 1992). Similarly a range of growth rate of 6–10 days (Kontoyiannis 1992; Lee and Cornillon 1996a) is chosen satisfactory for the model's performance. The model's growth rate decreases with increasing U_{SRG}^T for U_H^T up to 110 cm s^{-1}, beyond which it increases with increasing baroclinicity in the GS.

To understand the model dispersion, the phase-speed and growth-rate contours are superimposed on each other for the three pairs of variables. This is shown in Fig. 11. For analysis purposes, the wave-growth contours (dashed lines) are plotted within the range 6–10 days; the phase-speed contours are only shown between 8 and 12 km day^{-1}. Clearly, there is an available regime in which the feature model parameters (U_H^T, U_{SRG}^T, U_{SRG}^B) correspond to wave-growth characteristics well within the realistic observed range. These regimes are the shaded regions in Figs. 11a–c. The reasonable parameter variation ranges thus obtained from this figure are tabulated for the two limiting values of U_H^T (130 and 140 cm s^{-1}) in Table 3.

Figure 12 explains the results of the dispersion characteristic in shear space of the southern gyre. The bottom and the surface velocity of the southern gyre are plotted on the x axis and y axis, respectively. Two regimes of realistic phase speed and growth rate are identified as the two differently hatched regions corresponding to the two axis speeds (130 and 140 cm s^{-1}) at Cape Hatteras. Each constant shear line represents a specific pair of growth-rate and phase-speed values for a given U_H^T. The centerline of the region corresponding to $U_H^T = 130$ cm s^{-1} at Cape Hatteras depicts a growth rate (phase speed) of 8 days (10 km day^{-1}) and reflects a constant shear line of 5.25 cm s^{-1}. Similarly, the upper bound of the 140 cm s^{-1} region coincides with the upper bound of the 130 cm s^{-1} region corresponding to the 10 days (12 km day^{-1}) growth (speed) pair and represented by the 5.5 cm s^{-1} baroclinic shear of SRG.

Thus, we have established a realistic parameter variation regime for the two limiting axis speeds at Cape Hatteras. Note that any other speed between these limits similarly corresponds to a region in the shear space

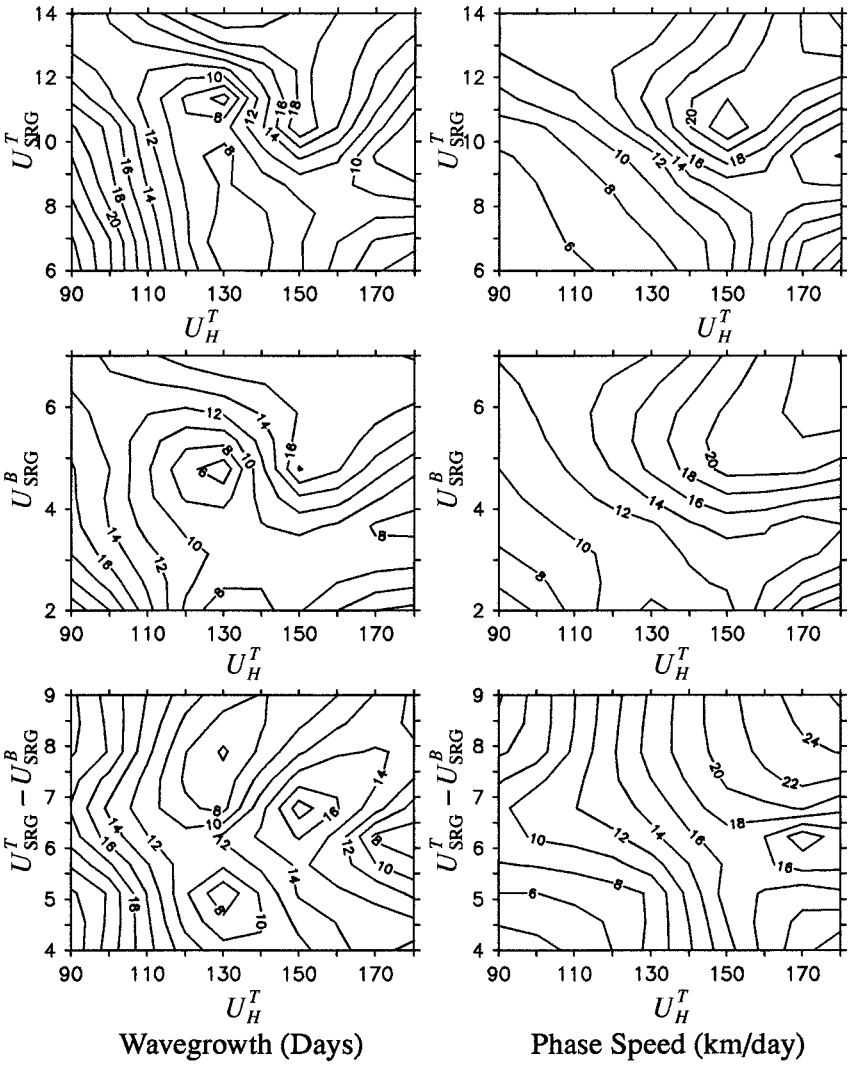

FIG. 10. Dispersion characteristics shown as a function of the GS top axis velocity at Cape Hatteras and the SRG parameters. The left panels are contours of wave growth, and the right panels are contours of phase speed. The *x* axis on all six panels is the GS axis speed (cm s^{-1}) at Cape Hatteras U_H^T. The other independent parameter is for (a) and (b) U_{SRG}^T, for (c) and (d) U_{SRG}^B, and for (e) and (f) $U_{\mathrm{SRG}}^T - U_{\mathrm{SRG}}^B$.

bounded by the upper limit of U_{SRG}^T and the lower limit of U_{SRG}^B to the top and left side of a similar quadrangle. The bottom-right corner of those quadrangles will lie on the line joining the two limiting values. This line is marked by crosses in Fig. 12. Any specific choice of SRG parameters for this regime would lead to realistic wave-growth and phase-speed characteristics between Cape Hatteras and the Grand Banks.

The individual realistic regimes for different axis velocities at Cape Hatteras are clearly shown in Fig. 13. Figure 13a shows the full regime—same as the large quadrangle in Fig. 12. Figures 13b–d show the regimes for three different values of U_H^T: 130, 135, and 140 cm s^{-1}. In these three plots, the corresponding top and bottom velocities of the GS at 60°W are also shown. These velocities are obtained using the numbers in Table 3 as well as Eqs. (24) and (25) of GRA. The range of maximum velocities for the Gulf Stream is obtained as 175–190 cm s^{-1}, which agrees well with observational studies listed in Table 1 of GRA. The maximum bottom velocity varies in the range between 10 and 18 cm s^{-1}, which is also reasonable from observational studies. It is important to note that the bottom line of the quadrangles in Fig. 13 always represent a growth rate (phase speed) of 6 days (8 km day^{-1}); the top line represents a pair of 10 days (12 km day^{-1}).

c. Variability of growth rate and phase speed

It is important to note that in this analysis, we find that increasing the shear of SRG, which is a measure

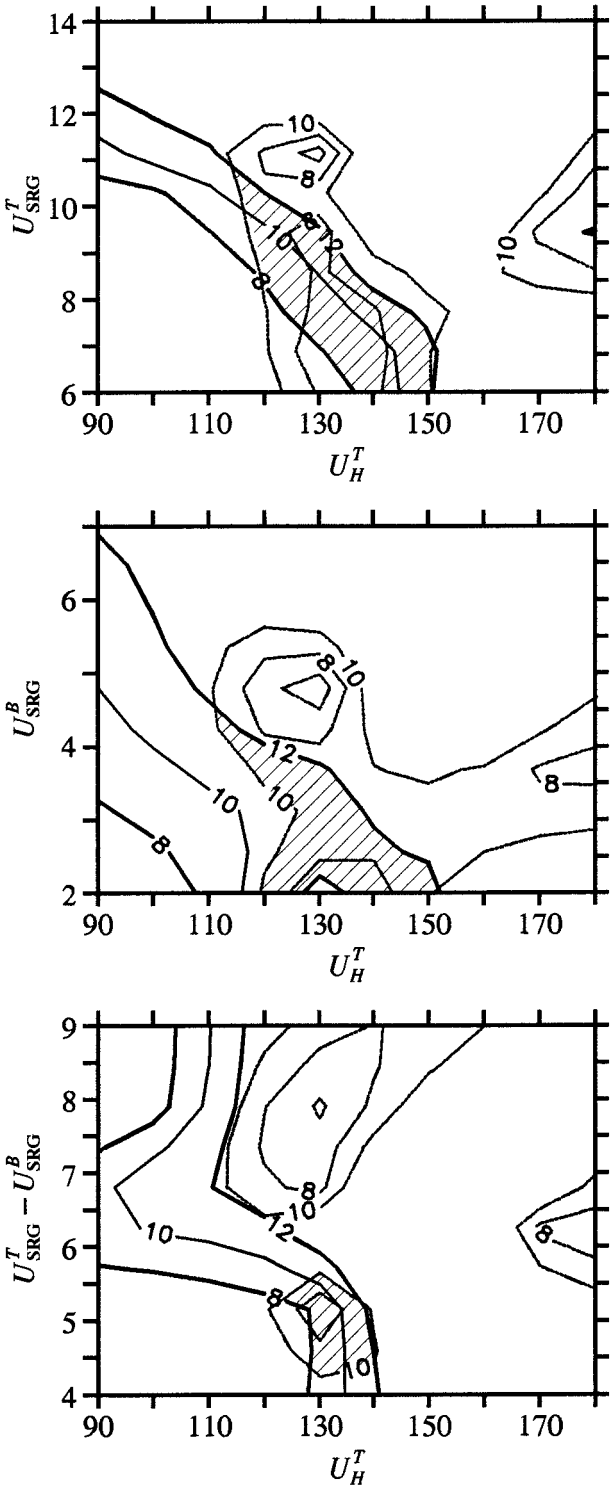

FIG. 11. Inference diagram: (a) U^T_{SRG}, (b) U^B_{SRG}, and (c) $U^T_{SRG} - U^B_{SRG}$ vs U^T_H. Wave-growth (dash) and phase-speed (solid) contours are superimposed together only within the observational range to infer the realistic parameter regime.

TABLE 3. Realistic ranges of multiscale parameters.

Shear at CH	ΔU^T_{SRG}	ΔU^B_{SRG}	Shear of SRG
120	8–10.5	3.5–4.25	6.5–8.5
130	7–10	2–4	5–5.5
140	6–8.5	2–3	4–5.5

of increasing baroclinicity in the GS, leads to larger growth rates and phase speeds. Similar increase is also seen with respect to increasing axis speed (or transport) at Cape Hatteras.

To the best of our knowledge, observational evidence in support of this behavior is not yet established. However, it is conceivable that when the transport is high, small-amplitude, short-wavelength meanders are simply subject to strong advection by the stream. This would result in faster phase speeds for the meanders in the region (74°–68°W) under consideration. It is difficult to resolve such variabilities in phase speed from IR imagery, which is often gappy over spatial and temporal bands (Lee and Cornillon 1996b).

It is also possible to speculate that a stream with larger transport, while advecting meanders, would slow the growth of meanders. Similarly, when the transport of the stream is relatively low, phase speeds would be slower, and growth will be magnified requiring less time to grow a comparable amplitude.

4. Dynamical behavior—Meanders and rings

In the previous section, we have established a realistic range of parameter variation that leads to realistic dispersion characteristics for the GSMR region. In this section, we discuss the behavior and sensitivity of the primitive equation dynamical model when integrated for the long term (12 weeks). The starting fields are obtained via slow-manifold QG initialization of the MSFMs. The axis speed of the GS at Cape Hatteras and the surface and bottom velocities of the SRG are varied

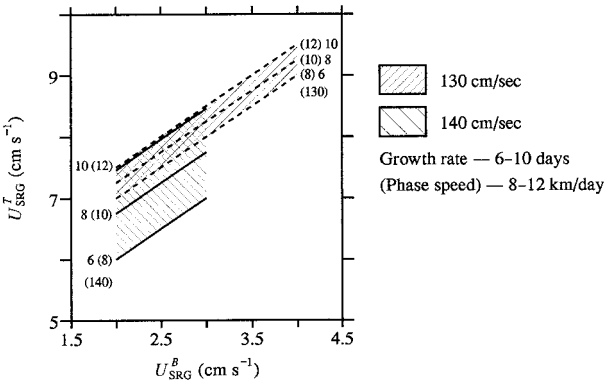

FIG. 12. Realistic parameter range in shear space. A composite picture of the dependence of realistic dispersion characteristics on the multiscale feature model parameters. Simplified reconstruction is shown in Fig. 13.

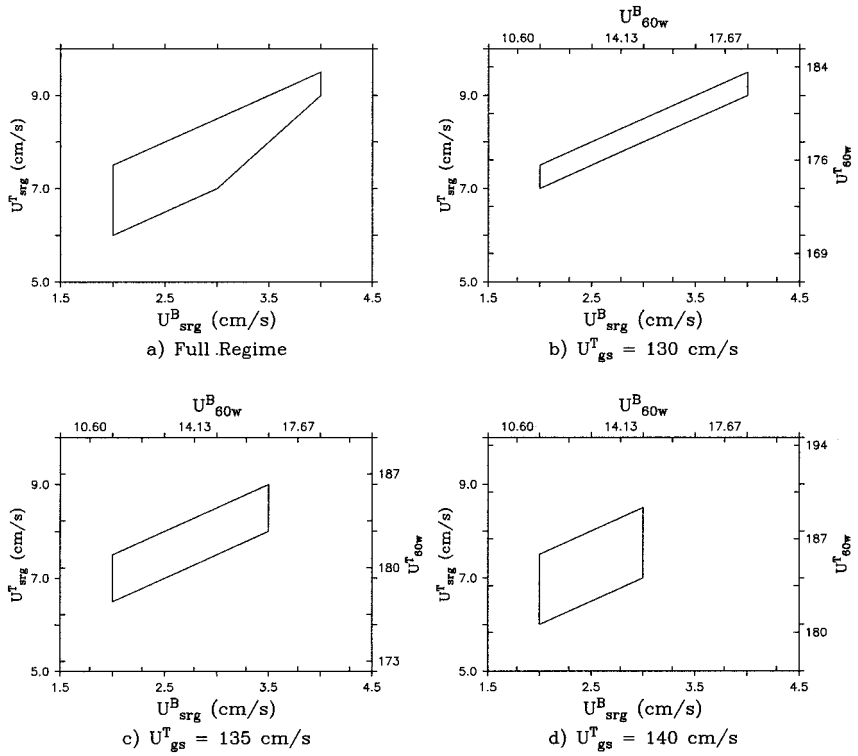

FIG. 13. Realistic parameter range for different axis velocities of the Gulf Stream at Cape Hatteras. (a) Full regime, (b) $U_H^T = 130$ cm s^{-1}, (c) $U_H^T = 135$ cm s^{-1}, and (d) $U_H^T = 140$ cm s^{-1}.

systematically within the range established in the previous section and shown in Fig. 12. After the initial wave growth in the first 3 weeks of simulations, meanders grow and finally detach from the stream to form rings during the second month, and thereafter meander–ring interactions are taking place. Such a general picture is quantified here in terms of several factors, such as maintenance of continuity of meandering throughout the domain and ability to form and reabsorb realistic rings at the observed rate.

Ten experiments were carried out within the realistic regime as depicted in Fig. 12. The chosen parameters of these experiments and the final results are presented in Table 4. In the following, we discuss the four cases that highlight most of the dynamical behaviors seen in the long-term simulations.

a. An example of a long-term simulation—Case 1 (130, 8.25, 3.0)

Here, we describe the dynamical behavior of the 12-week-long simulation with parameters listed in Table 4 for U_H^T, U_{SRG}^T, and U_{SRG}^B; the remaining parameters are listed in Table 1. This case will be referred to as case 1 in later sections.

The mean recirculation gyres interact with the meandering of the GS, and mesoscale recirculations centered at the crests and troughs of the propagating me-

TABLE 4. Long-term simulations—sensitivity studies.

Shear at CH (cm s^{-1})	U_{SRG}^T (cm s^{-1})	U_{SRG}^B (cm s^{-1})	$T_{60\mathrm{W}}$ (Sv)	Days per event (30–84)	Comments
130	7.0	2.0	152	9	Lower transport
130	7.5	2.5	158	8–6	Large meanders
130	8.25	3.0	165	7.7	Marginal
130	8.75	3.5	171	7.7	Strong WCR
130	9.25	4.0	177	6	Unrealistic rings
135	7.0	2.0	156	8	Large meanders
135	7.5	3.0	166	7.7	Standard transport
140	6.0	2.0	154	8–6	Distorted meanders
140	7.0	2.5	163	7.5	Marginal
140	8.0	2.75	169	8	Higher transport

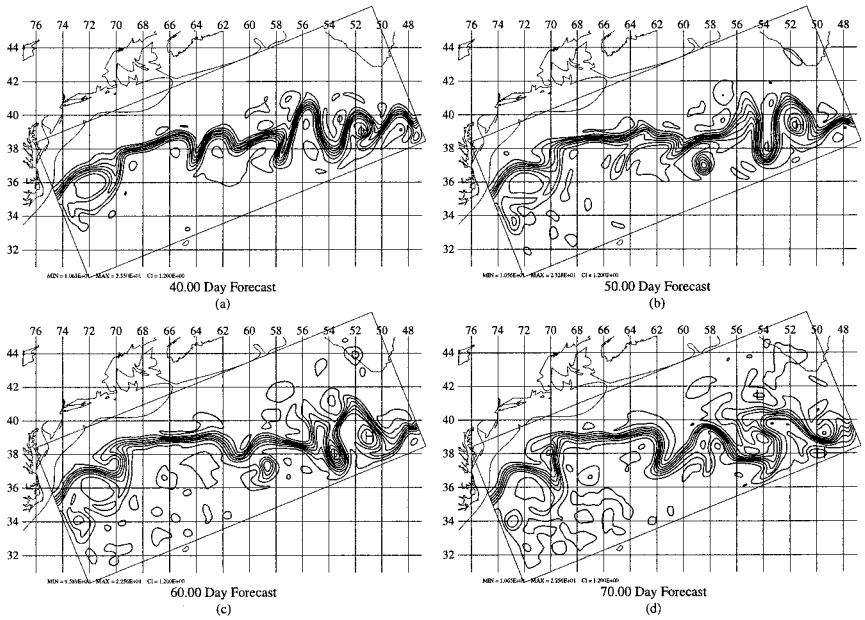

FIG. 14. Long-term PE simulations—case 1: (130, 8.25, 3.0).

anders are formed. Such smaller-scale recirculations were observed by Bower and Rossby (1989) and studied by Rossby (anatomy experiment). Such scale-to-scale interactions occur after the initial wave growth has taken place during the first 3 weeks of simulation. Once the rings are formed (after day 40) such mesoscale–subbasin-scale interactions are dominated by mesoscale activity, while the subbasin-scale features dominate the far away regions to the south and west side of the domain.

The evolution of the GS is shown in Fig. 14 at every 10-day interval between days 40 and 70. Along the path of the GS, the first trough is formed at around 69°–70°W, which is observed in reality at 68°–67°W during the SYNOP experiment (Johns et al. 1995; Watts et al. 1995). The exact cause behind the stream's preference to form a trough there is still unknown, although the two simulations we presented in section 2c suggest that the interaction of DWBC and the GS may play a role in determining the exact location of the trough.

In the region 70°–65°W, the stream stays remarkably coherent and free from large-amplitude meandering throughout the simulation over 12 weeks. Furthermore, such realistic behavior is maintained for other simulations as well. Beyond 65°W, the second trough is formed, presumably due to topographic interactions with the New England Seamounts. The formation of this trough at 64°W by day 40 is followed by a meander whose trough at 57°W detaches from the stream on day 46. This ring is clearly seen in Fig. 14b. The size and strength of the cold ring matches well with Gulfcast data. The ring formed at 58°W is about 100 km in radius with a 5°C temperature difference between its core and the Sargasso Sea. The trough at 64°W grows and detaches from the stream on day 52 to form an elliptical cold core ring. This is a weaker ring than the previous one at 59°W, and it propagates to the west at 6 km day^{-1} through the simulation. This ring finally interacts with the trough at 70°W beyond day 86 (not shown here).

The region east of 57°W is where the subbasin-scale gyres extract mass out from the GS. In the model simulations, we see large-amplitude meanders forming in this region, which is consistent with observations (Hogg 1983; Hogg et al. 1986). The large trough formed just east of 54°W elongates to almost detach a ring by day 60 after which it interacts with model boundary at the southern edge (see Fig. 14c.). The meander to the west of this trough, however, interacts with this ring and reabsorbs it to form a large meandering stream between 56° and 52°W (Fig. 14d). Meanwhile, a warm core ring is formed at 55°W from the interaction between the eastward propagating meander and the cold core ring. This warm core ring is seen interacting with the crest at 54°W in Fig. 14d. Beyond day 70, mesoscale activity seems to increase, and no more events are studied for the purpose of quantifying the dynamical behavior.

Note that a cyclonic feature detaches from the trough at 70°W (days 50–70), propagates westward, and interacts with the western boundary of the domain. Since the model maintains the boundary condition over the simulation time period, such propagation seemingly results as a cold-core-ring-like feature just south of the inlet of the stream. This is an artifact of the boundary condition implementation in the numerical model and would not be a dynamically existing feature if a radiation boundary condition was implemented. We have excluded all such features and/or events that could be

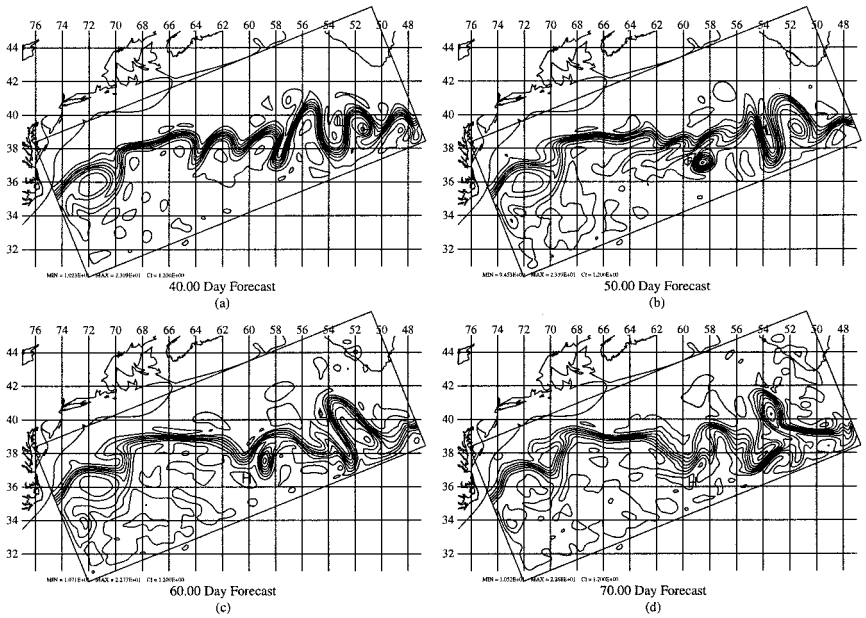

FIG. 15. Long-term PE simulations—case 2: (130, 9.25, 4.0).

boundary influenced while determining the statistics of the ring formation–reabsorbtion behavior.

A cold core ring forms on day 44 at 51°W (the elongated trough is seen at day 40) and gets reabsorbed in the recirculating region centered at 39.2°N, 51.5°W. This event is well beyond the influence regime of the boundary. By day 50, one can see only traces of this ring in the strong recirculation. Taking a census of rings formed and reabsorbed during the simulation period when mesoscale activity begins, that is, between days 30 and 84, we find a total of five births and two reabsorptions—which is equivalent to about 8 days per event. This compares well with the observed rate of 8.6 days per event during the Gulfcast (Robinson et al. 1989; Glenn and Robinson 1995) experiment.

b. Effect of transport variation (130, 9.25, 4.0)

In this case, we increase the maximum transport of the stream by 12 Sv through both baroclinic and barotropic flux increases from the SRG. This is done to be consistent with the realistic wave-growth regime. It is important to note that similar events happen in this simulation as in case 1; however, we will elaborate the differences found hereafter. The temperature fields at 10-day intervals between days 40 and 70 are shown in Fig. 15.

The meanders are found to be a little tighter in this simulation than in case 1. The cold core ring at 63°W is more diamond-shaped than elliptical. This ring interacts with the stream and gets reabsorbed by day 72 before being reborn on day 80. The trough at 54°W does not result in a cold ring in this case in contrast to case 1. In fact, this trough interacts with the southern boundary of the domain, and the following meander, as a result of which a warm core ring is formed around day 70 at 54°W. This development is very different from the one in case 1, in which the process of another cold ring is formed on day 68. The warm and cold core rings interact with the meandering stream and generate vigorous meso- and submesoscale features later in the simulation beyond day 80.

c. Effect of shear variation at Cape Hatteras (140, 7, 2.5)

In this particular case, the effect of increased shear (U_H^T) at Cape Hatteras on the ring formation behavior is studied. An increased shear of 140 cm s^{-1} is chosen in this case along with values of $U_{\mathrm{SRG}}^T = 7.0$ cm s^{-1} and $U_{\mathrm{SRG}}^B = 2.5$ cm s^{-1} to be consistent with the realistic growth regime in Fig. 12. Such a choice of parameters result in a GS maximum transport of 161 Sv, which is comparable to that of 165 Sv in case 1.

The results of this simulation between days 40 and 70 are presented in Fig. 16 at every 10-day interval. In this simulation, increased mesoscale activity in the southwestern side of the domain is very evident by day 40. Such increase in activity is a direct result of an interaction of a stronger jet with the SBS SRG than in case 1. This activity is seen to develop slowly after the initial wave-growth period of 3 weeks. Similar to case 1, the three regions (64°, 55°, and 51°W) are the latitudes along the stream path, where three cold rings are formed during this simulation. However, it is interesting to note that the ring at 63°W is stronger than the one in case 1, and the ring at 55°W is weaker than the corresponding one in case 1. The ring at 51°W is well defined by day

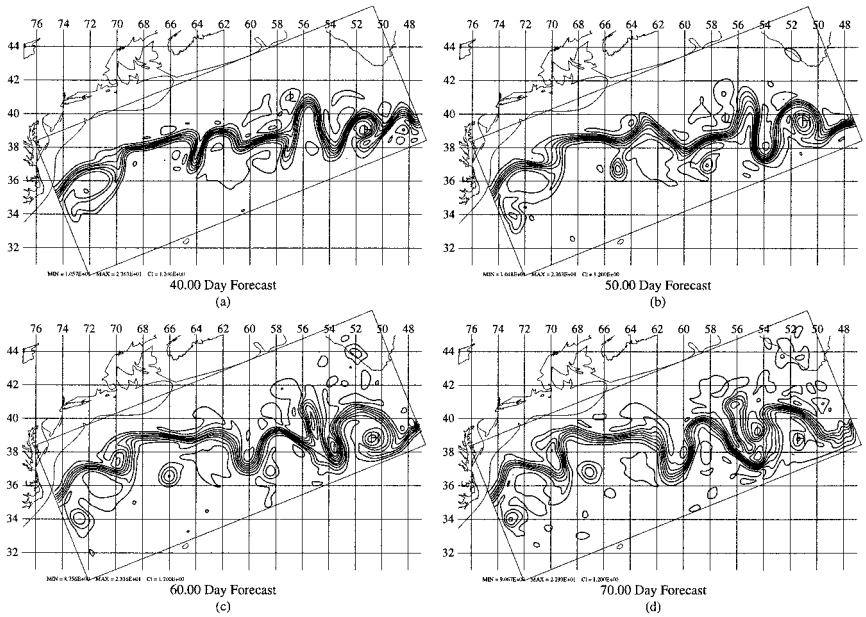

FIG. 16. Long-term PE simulations—case 3: (140, 7, 2.0).

42, although it merges with the recirculating cell centered at 39.5°N, 51°W by day 48.

At 70°W, the meander is found to loop northwestward to develop a crest by day 50. This crest finally detaches into a warm ring by day 70. Between days 50 and 70 the stream maintains its continuous path up to 56°W very well. Between 56° and 53°W, a warm and cold core ring combination is seen to hold together from day 54 to day 64. Beyond day 64, the cold core is finally absorbed by the stream; the warm core ring forms into a multiple center elongated feature. Later in the simulation, the northern part of the feature becomes a well-defined warm core ring and starts propagating westward. Both of the rings formed at 63° and 55°W propagate westward at about 6 km day^{-1} before finally interacting with the stream later in the simulation beyond day 70.

d. A quasigeostrophic example (130, 8.25, 3)

The initial wave-growth characteristics are similar for both the QG and the PE dynamics. However, in the case of QG simulations, the realistic wave growth is achieved earlier in the dynamical integration starting from the same initialization. Here, we discuss the long-term simulation of the initialization with parameter values in case 1. The results are shown in Fig. 17 for this case. The streamfunction fields at 50 m are comparable to the temperature field for the primitive equation simulation. The dynamically simulated streamfunction fields at 50 m are shown for days 30 through 60 at 10-day intervals.

Similar to case 1, a cold ring at 63°W is formed on day 28, which gets reabsorbed in the stream by day 40. Another cold ring is formed at 51°W by day 38 and propagates westward before finally being reabsorbed by the stream between day 64 and 70 at 52°W. In contrast to the PE simulation, a warm core ring tends to form at 57°W, but before finally detaching from the stream it gets reabsorbed in the stream. Similar evolution is again observed during days 48–54. This time, however, the warm core ring is able to hold its identity separate from the stream while still interacting with it before finally detaching on day 64.

The activity rate of this simulation is about 8.6 days per event, which agrees well with observations. It is important to note that the QG simulation has very well defined recirculation cells on the slope side of the stream between crests. The stream paths, as defined by the constant streamlines, are generally smoother than their isothermal counterparts for the PE simulations.

e. Transport variability constraints and final selections

From observational studies, it is known that the transport of the Gulf Stream has considerable seasonal to interannual variability. Similar variability is also observed in the Sargasso Sea. Using such information, we are now in a position to further constrain the parameter space based on model behavior results presented in Figs. 12 and 13, and Table 4. Our objective here is to identify a set of transport-dependent parameter values that would enable the dynamical models reproduce the most realistic dispersion and dynamical behavior. To do this, we chose a higher transport scenario, a lower transport scenario, and a standard transport scenario. Note that two other simulations (experiments 10 and 1) relevant to higher and lower transport scenarios, respectively, are presented in Figs. 18 and 19 at 10-day intervals.

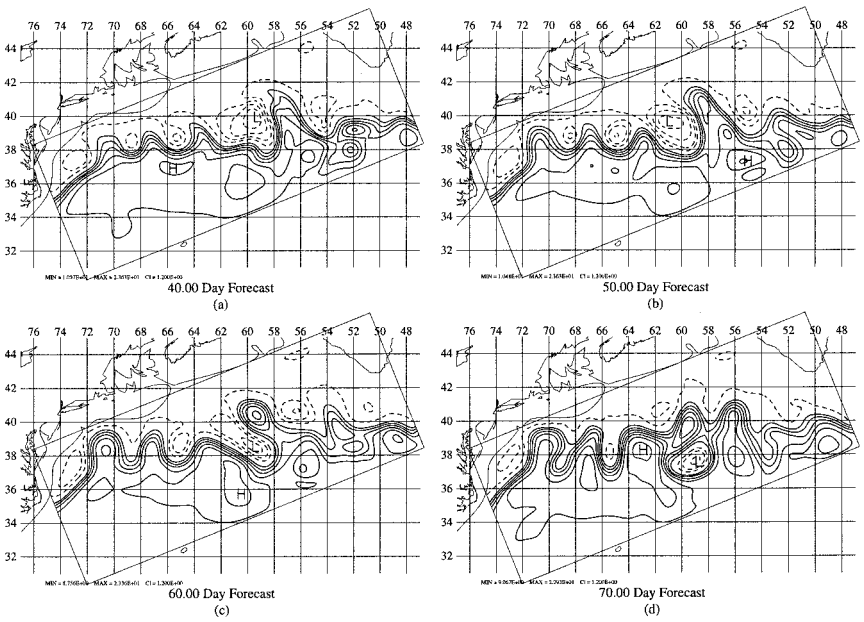

FIG. 17. Long-term QG simulations—case 4: (130, 8, 2.5).

Clearly, our choice for the maximum axis speed (corresponding to higher transport scenario) at Cape Hatteras is 140 cm s^{-1}, which results in a GS transport of 77 Sv. The contribution from the SRG has also been assumed to be higher, restricting our choice to the upper half of the quadrangle identified for this particular speed in Fig. 13d. This higher transport regime is shown in Fig. 20a. In this restricted regime, the last case (experiment 10 in Table 4) behaved reasonably well dynamically with an event rate of almost 8 days per event. Also, in this case realistic cold and warm core rings were formed and reabsorbed (see Fig. 18). This choice of parameters (U_H^T = 140 cm s^{-1}, U_{SRG}^T = 8.0 cm s^{-1}, U_{SRG}^B = 2.75 cm s^{-1}) yields a maximum transport of 169 Sv at 60°W for the GS.

Similarly, the lower transport GS is modeled by

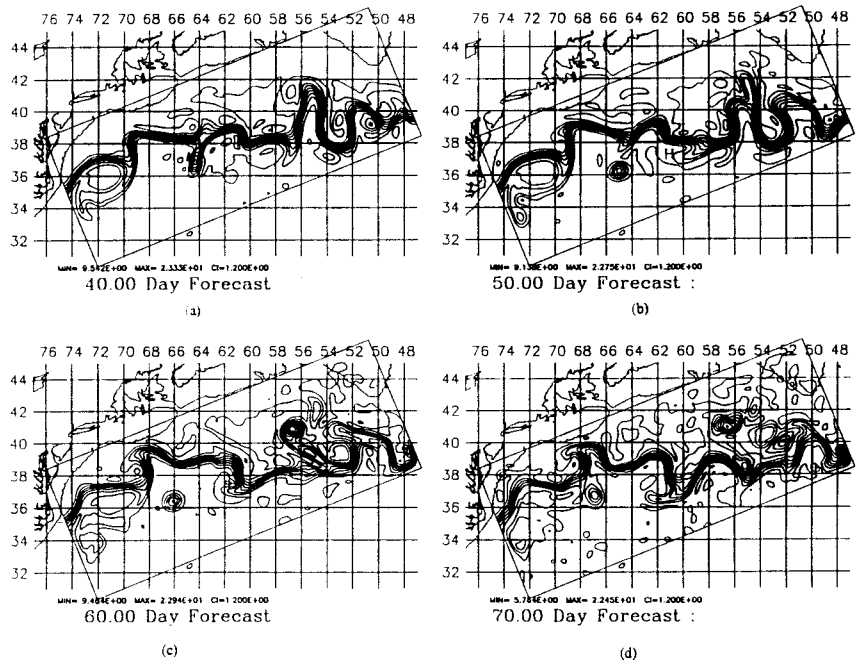

FIG. 18. Long-term PE simulations—experiment 10: (140, 8, 2.75).

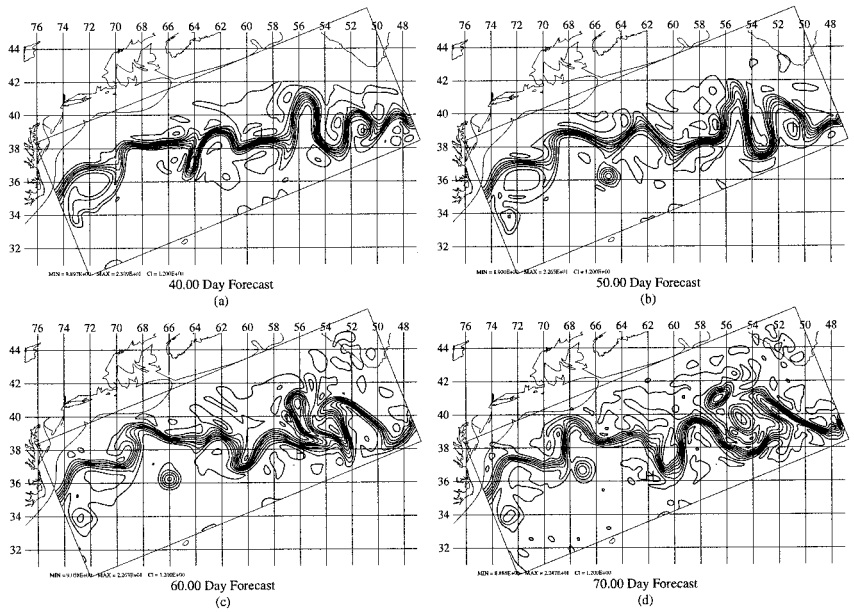

FIG. 19. Long-term PE simulations—experiment 1: (130, 7, 2.0).

choosing 130 cm s^{-1} as the surface axis speed at Cape Hatteras. The corresponding transport of 70 Sv is modified downstream with the lowest influx from the SRG. Thus, we now restrict our attention to the left-lower half of the region shown in Fig. 13b, which is separately shown in Fig. 20b. In this region, two cases (experiments 1 and 2 in Table 4) performed dynamically very well. However, since experiment 2 develops large-amplitude meanders beyond day 65 into the simulation, we choose experiment 1 as our lower transport set of parameters. This choice of parameters (U_H^T = 130 cm s^{-1}, U_{SRG}^T = 7.0 cm s^{-1}, U_{SRG}^B = 2.0 cm s^{-1}) yields a maximum transport of 152 Sv at 60°W for the GS. The simulation fields at every 10-day interval are shown in Fig. 19.

It is interesting to note here that the two regimes are limited by two different sets of phase-speed and growth-rate numbers. The higher transport regime (Fig. 20a) corresponds to the faster (larger) phase speed (growth rate) of 10–12 km day^{-1} (8–10 days). Similarly, the lower transport regime (Fig. 20b) corresponds to the slower (smaller) phase-speed (growth rate) range. The transition between these two limiting choices are selected based on their transport and dynamical behavior. Two more experiments (3 and 7) are thus identified as possible choices for the standard transport transition periods. However, the parameters for experiment 3 (130, 8.25, 3) do not allow for smooth transition between the two sets of parameters. Thus, we chose the parameters for experiment 7 (135, 7.5, 3) as our calibrated set for the standard transport case. These three sets of parameters are being extensively used for synoptic forecasting and assimilation studies in this region. The results of such studies will be discussed in a forthcoming paper.

5. Summary and conclusions

The numerical dynamical models, both primitive equation and quasigeostrophic, have been tuned and calibrated to realistic wave-growth and dynamical behavior in the GSMR (Gulf Stream and meander ring) region. The dispersion characteristics, namely, the observed wave-growth rate of 6–10 days is attainable by using a combination of values for three parameters: the shear at Cape Hatteras as well as the top and bottom velocities of the southern recirculation gyre. Similar combinations of parameters also yield the observed range of phase speed (8–12 km day^{-1}). Long-term simulations using both primitive equation and quasigeostrophic dynamical models were carried out within these realistic regimes of parameter variation to study the ring formation and reabsorption behavior. Both of the dynamical models evolve at a rate of about 8–9 days per event, which is agreeable to observational studies in this region. Based on the observed variability of transport of the GS, we have also identified three sets of parameters for different seasons to be used for realistic nowcasting and forecasting.

Such dynamically tuned, realistic model sets can now be used for further scientific process studies dealing with interaction between different features of the GSMR region, or scale-to-scale interactions and transfer processes, ring formation studies, etc. Also, these calibrated dynamical models are very useful for realistic forecast in a limited oceanic region and for data assimilation studies, which will be discussed in Part III (Gangopadhyay and Robinson 1997). Together with Part I of this study, a complete methodology for obtaining a kinematically adjusted initialization, and using such initial-

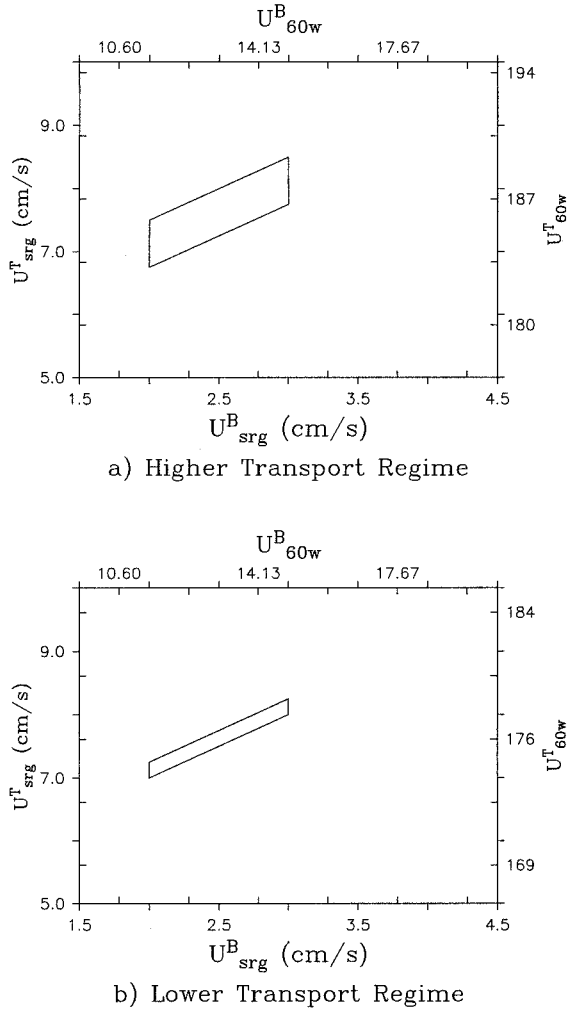

FIG. 20. Transport constrained realistic regimes: (a) higher transport regime and (b) lower transport regime.

izations to dynamically tune and statistically verify a particular model set, has been successfully developed for the western North Atlantic.

Acknowledgments. This study was supported by the Office of Naval Research (N00014-93-1-0577) through a contract to Harvard University. We are grateful to Drs. Carlos Lozano and Hernan Arango for their helpful discussions on numerical modeling issues. Some helpful discussions with Drs. R. Watts and T. Lee are greatly appreciated. Short- and long-term simulations were carried out at the large-scale supercomputer center at Stennis and at the Pittsburg Supercomputer Center. We would also like to thank Ms. Marsha Cormier, Mr. Wayne G. Leslie, and other members of the Harvard University Oceanography group for their support of this work at numerous instances.

REFERENCES

Bower, A. S., and H. T. Rossby, 1989: Evidence of cross-frontal exchange processes in the Gulf Stream based on isopycnal RAFOS float data. *J. Phys. Oceanogr.,* **19,** 1177–1190.

Ezer, T., and G. L. Mellor, 1992: A numerical study of the variability and the separation of the Gulf Stream, induced by surface atmospheric forcing and lateral boundary flows. *J. Phys. Oceanogr.,* **22,** 660–682.

Flierl, G. R., 1991: Dispersion relations—Theory. *Synoptician,* **2** (1), 3–4.

Gangopadhyay, A., and A. R. Robinson, 1997: Circulation and dynamics of the western North Atlantic. Part III: Forecasting the meanders and rings. *J. Atmos. Oceanic Technol.,* **14,** 1352–1365.

——, P. Cornillon, and L. B. Jackson, 1987: Spectral analysis of GS meanders. *Eos Trans. AGU Spring Meeting,* Baltimore, MD.

——, A. R. Robinson, and H. G. Arango, 1997: Circulation and dynamics of the western North Atlantic. Part I: Multiscale feature models. *J. Atmos. Oceanic Technol.,* **14,** 1314–1332.

Gilman, C., 1988: A study of the Gulf Stream downstream of Cape Hatteras, 1975–1986. M.S. thesis, Dept. of Physical Oceanography, University of Rhode Island, 75 pp. [Available from Graduate School of Oceanography, University of Rhode Island, Narragansett, RI 02882.]

Glenn, S. M., and A. R. Robinson, 1990: Nowcasting and forecasting of oceanic dynamic and acoustic fields. *Computational Acoustics: Ocean-Acoustic Models and Supercomputing,* D. Lee, A. Cakmak, and R. Vichnevetsky, Eds., North-Holland, 117–128.

——, and ——, 1995: Validation of an operational Gulf Stream forecasting model. *Qualitative Skill Assessment for Coastal Models,* AGU Estuarine/Coastal Series, American Geophysical Union, Vol. 47, 469–499.

——, D. L. Porter, and A. R. Robinson, 1991: A synthetic geoid validation of GEOSAT mesoscale dynamic topography in the Gulf Stream region. *J. Geophys. Res.,* **96,** 7145–7166.

Haidvogel, D. B., J. Wilkins, and R. E. Young, 1991: A semi-spectral primitive equation coastal circulation model using vertical sigma and horizontal curvilinear coordinates. *J. Comput. Phys.,* **94,** 151–185.

Halkin, D., and H. T. Rossby, 1985: The structure and transport of the Gulf Stream at 73°W. *J. Phys. Oceanogr.,* **15,** 1439–1452.

Hogg, N. G., 1983: A note on the deep circulation of the western North Atlantic: Its nature and causes. *Deep-Sea Res.,* **30,** 945–961.

——, and H. Stommel, 1985: On the relationship between the deep circulation and the GS. *Deep-Sea Res.,* **32,** 1181–1193.

——, R. S. Pickart, R. M. Hendry, and W. J. Smethie Jr., 1986: The northern recirculation gyre of the GS. *Deep-Sea Res.,* **33,** 1139–1165.

Johns, W. E., T. J. Shay, J. M. Bane, and D. R. Watts, 1995: Gulf Stream structure, transport, and recirculation near 68°W. *J. Geophys. Res.,* **100,** 817–838.

Kontoyiannis, H., 1992: Variability of the Gulf Stream path between 74°W and 70°W: Observations and quasi-geostrophic modeling of mixed instabilities. Ph.D. thesis, University of Rhode Island, 129 pp. [Available from Graduate School of Oceanography, University of Rhode Island, Narragansett, RI 02882.]

Lai, C. A., W. Qian, and S. M. Glenn, 1994: Data assimilation and model evaluation experiment datasets. *Bull. Amer. Meteor. Soc.,* **75,** 793–810.

Lee, T., and P. Cornillon, 1996a: Propagation of Gulf Stream meanders between 74°W and 70°W. *J. Phys. Oceanogr.,* **26,** 205–224.

——, and ——, 1996b: Propagation and growth of Gulf Stream meanders between 75°W and 45°W. *J. Phys. Oceanogr.,* **26,** 225–243.

Mellor, G. L., and T. Ezer, 1991: A Gulf Stream model and an altimetry assimilation scheme. *J. Geophys. Res.,* **96,** 8779–8794.

Pickart, R. S., and W. M. Smethie Jr., 1993: How does the western boundary current cross the Gulf Stream? *J. Phys. Oceanogr.,* **23,** 2602–2616.

Robinson, A. R., S. M. Glenn, M. A. Spall, L. J. Walstad, G. M. Gardner, and W. G. Leslie, 1989: Forecasting Gulf Stream meanders and rings. *EOS, Oceanogr. Rep.,* **70** (45), 1464–1473.

Sato, O. T., and H. T. Rossby, 1992: Seasonal and secular variability of the GS. *Synoptician,* **3**(5), 1–4.

Shapiro, R., 1970: Smoothing, filtering and boundary effects. *Rev. Geophys. Space Phys.,* **8,** 359–387.

——, 1971: The use of linear filtering as a parameterization of atmospheric diffusion. *J. Atmos. Sci.,* **28,** 523–531.

Spall, M. A., and A. R. Robinson, 1989: A new open ocean, hybrid coordinate primitive equation model. *Math. Comput. Simulation,* **31,** 241–269.

——, and ——, 1990: Regional primitive equation studies of the Gulf Stream meander and ring formation region. *J. Phys. Oceanogr.,* **20,** 985–1016.

Tracey, K. L., and D. R. Watts, 1986: On Gulf Stream meander characteristics near Cape Hatteras. *J. Geophys. Res.,* **91,** 7587–7602.

Vazquez, J., and D. R. Watts, 1985: Observations on the propagation, growth, and predictability of Gulf Stream meanders. *J. Geophys. Res.,* **90,** 7143–7151.

Watts, D. R., 1983: Gulf Stream variability. *Eddies in Marine Science,* A. R. Robinson, Ed., Springer-Verlag, 114–144.

——, K. L. Tracey, J. M. Bane, and T. J. Shay, 1995: Gulf Stream path and thermocline structure near 74°W and 68°W. *J. Geophys. Res.,* **100,** 18 291–18 312.

Willems, R. C., and Coauthors, 1994: Experiment evaluates ocean models and data assimilation in the Gulf Stream. *Eos, Trans. Amer. Geophys. Union,* **75,** 385–394.

Worthington, L. V., 1976: On the North Atlantic circulation. *Johns Hopkins Oceanogr. Studies Monogr.,* No. 6, The Johns Hopkins University Press, 110 pp.